J|A|C|S ARTICLES

Published on Web 06/02/2010

Alkaline Beryllium Borate $NaBeB_3O_6$ and $ABe_2B_3O_7$ (A = K, Rb) as UV Nonlinear Optical Crystals

Shichao Wang, Ning Ye,* Wei Li, and Dan Zhao

Key Laboratory of Optoelectronic Materials Chemistry and Physics, Fujian Institute of Research on the Structure of Matter, Chinese Academy of Sciences, Fuzhou, Fujian 350002, P. R. China

Received April 1, 2010; E-mail: nye@fjirsm.ac.cn

Abstract: A new series of alkaline beryllium borates $NaBeB_3O_6$, α-$KBe_2B_3O_7$, β-$KBe_2B_3O_7$, γ-$KBe_2B_3O_7$, and $RbBe_2B_3O_7$ were synthesized by spontaneous crystallization with molten fluxes based on $A_2O-B_2O_3$ (A = Na, K, Rb) solvent. For $KBe_2B_3O_7$, three polymorphous phases were found and are referred to as α-, β-, and γ-$KBe_2B_3O_7$ relative to their crystallization temperature from high to low. All of the materials are noncentrosymmetric except α-$KBe_2B_3O_7$. $NaBeB_3O_6$ and α-$KBe_2B_3O_7$ consist of a new anionic group $[Be_2B_3O_{11}]^{9-}$, which is similar to a naphthalene molecule that is rarely found in inorganic matter. β-$KBe_2B_3O_7$, γ-$KBe_2B_3O_7$, and $RbBe_2B_3O_7$ consist of 2D alveolate beryllium borate layers $[Be_2BO_5]_\infty$, which are connected by strong covalent bonds. The UV−vis diffuse reflectance spectroscopy on powder samples indicated that the short-wavelength absorption edges of noncentrosymmetric materials are all below 200 nm. Second-harmonic generation (SHG) on powder samples was measured using the Kurtz and Perry technique, which indicated that $NaBeB_3O_6$, β-$KBe_2B_3O_7$, γ-$KBe_2B_3O_7$, and $RbBe_2B_3O_7$ are all phase matchable materials, and their measured SHG coefficients were approximately 1.60, 0.75, 0.68, and 0.79 times as large as that of d_{36} (KDP), respectively.

1. Introduction

Deep ultraviolet (deep UV) coherent light wavelengths below 200 nm have become increasingly important and are attracting more attention because of their promising applications, such as in semiconductor photolithography, laser micromachining, photochemical synthesis, material processing, and superhigh-resolution as well as angle-resolved photoemission spectroscopy. The best way to produce deep UV coherent light with solid-state lasers is through cascaded frequency conversion using deep UV nonlinear optical (NLO) crystals. However, it is a particularly difficult challenge to have suitable materials that possess high NLO coefficients and wide UV transparency.

Over the past three decades, many efforts have been made to understand the relationship between the composition, structure, and NLO properties of crystals, which are critical in the development of new NLO crystals. According to the Anionic Group Theory proposed by Chen,[1−3] the overall nonlinearity of crystal is the geometrical superposition of the microscopic second-order susceptibility of the NLO-active anionic groups (structural units). Favorable structural units in inorganic compounds with large nonlinear susceptibilities are, for example, planar $[BO_3]^{3-}$ with a π-conjugated system, polar ionic groups including an asymmetric metal-oxide polyhedron, and coordination units with a lone-pair cation.[4−8] In addition to the microscopic nonlinear susceptibilities of the NLO-active structural units, the orientation of these structural units and their number density influence the bulk NLO properties as well. For example, a higher density of the NLO-active structural units together with their coparallel alignment in the crystal structure is thought to produce higher bulk nonlinear coefficients. The ongoing intensive studies on borate anionic groups have resulted in the discovery of many new UV transparent NLO borates that include β-BaB_2O_4 (BBO)[9] with the anionic groups $[B_3O_6]^{3-}$, LiB_3O_5 (LBO),[10] CsB_3O_5 (CBO),[11] and $CsLiB_6O_{10}$ (CLBO)[12,13] with $[B_3O_7]^{5-}$.

Borate frameworks and building blocks are usually constructed using planar $[BO_3]$ triangles and tetrahedral $[BO_4]$ polyhedra. The substitution of a $[BeO_4]$ tetrahedron, a deep UV transparent structural unit, for $[BO_4]$ may potentially lead to new NLO-active beryllium borate anionic groups and various types of framework connections, which may promote further development of novel UV NLO materials. Based on a theoretical study, Li[14] has proposed that beryllium borates possess the largest energy gap among all alkaline and alkaline earth borates

(1) Chen, C. *Sci. Sin. (Engl. Ed.)* **1979**, *22*, 756.
(2) Chen, C. T.; Liu, G. Z. *Annu. Rev. Mater. Sci.* **1986**, *16*, 203.
(3) Chen, C. T.; Wu, Y. C.; Li, R. K. *Int. Rev. Phys. Chem.* **1989**, *8*, 65.
(4) Pan, S.; Smit, J. P.; Watkins, B.; Marvel, M. R.; Stern, C. L.; Poeppelmeier, K. R. *J. Am. Chem. Soc.* **2006**, *128*, 11631.
(5) Chang, H. Y.; Kim, S. H.; Halasyamani, P. S.; Ok, K. M. *J. Am. Chem. Soc.* **2009**, *131*, 2426.
(6) Chang, H. Y.; Kim, S. H.; Ok, K. M.; Halasyamani, P. S. *J. Am. Chem. Soc.* **2009**, *131*, 6865.
(7) Chang, H. Y.; Kim, S. H.; Ok, K. M.; Halasyamani, P. S. *Chem. Mater.* **2009**, *21*, 1654.
(8) Sun, C. F.; Hu, C. L.; Xu, X.; Ling, J. B.; Hu, T.; Kong, F.; Long, X. F.; Mao, J. G. *J. Am. Chem. Soc.* **2009**, *131*, 9486.
(9) Chen, C. T.; Wu, B. C.; Jiang, A. D.; You, G. M. *Sci. Sin., Ser. B* **1985**, *28*, 235.
(10) Chen, C. T.; Wu, Y. C.; Jiang, A. D.; Wu, B. C.; You, G. M.; Li, R. K.; Lin, S. J. *J. Opt. Soc. Am. B* **1989**, *6*, 616.
(11) Wu, Y. C.; Sasaki, T.; Nakai, S.; Yokotani, A.; Tang, H. G.; Chen, C. T. *Appl. Phys. Lett.* **1993**, *62*, 2614.
(12) Mori, Y.; Kuroda, I.; Nakajima, S.; Sasaki, T.; Nakai, S. *Appl. Phys. Lett.* **1995**, *67*, 1818.
(13) Tu, J. M.; Keszler, D. A. *Mater. Res. Bull.* **1995**, *30*, 209.
(14) Li, R. K. *J. Non-Cryst. Solids* **1989**, *111*, 199.

and, hence, the shortest transmission cutoff wavelength in the UV region. Due in part to the high toxicity of the Be compounds used as starting materials during preparation, relatively few synthetic beryllium borate compounds are known, which include $MBe_2B_2O_6$[15,16] (M = Sr and Ba), $CaBeB_2O_5$,[17] $Li_{14}Be_5B(BO_3)_9$,[18] and $RbBe_4B_3O_9$,[19] all of which have been found to crystallize in centrosymmetric space groups.

Typical examples of beryllium borate frameworks are the two-dimensional (2D) $[Be_2BO_3O_2]_\infty$ or $[Be_2BO_3F_2]_\infty$ layers that can be found in hydrated beryllium borate $Be_2BO_3OH\cdot H_2O$,[20,21] fluoroberyllium borate Be_2BO_3F,[22] and $ABe_2BO_3F_2$ (A = Na, K, Rb, Cs, and Tl)[23−27] among which KBBF ($KBe_2BO_3F_2$)[28] has been shown to be the best material for deep UV applications and is the only material that can generate coherent light at 170 nm by direct second-harmonic generation. The NLO properties, birefringence, and band gap in KBBF crystals are mainly determined by the identical direction of $[BO_3]^{3-}$ groups in the $[Be_2BO_3F_2]_\infty$ layers extending infinitely in the $a-b$ plane. However, this crystal has a very strong layer habit with respect to crystal growth due to the relatively weak $F^-\cdots K^+$ ionic interactions between the adjacent $[Be_2BO_3F_2]_\infty$ layers along the *c*-axis. As a result, it may be feasible to grow deep UV NLO crystals through covalent bonding of the adjacent $[Be_2BO_3O_2]_\infty$ or $[Be_2BO_3F_2]_\infty$ layers. Although alkaline earth beryllium borates $M_2Be_2B_2O_7$[29−31] (M = Sr and Ba) consist of $[Be_3B_3O_6]_\infty$ 2D layers bridged by oxygen atoms bound to Be atoms, their structures were not fully determined; moreover, the optical uniformities of their crystals were found to be very poor.[32]

Although many new beryllium borate frameworks were obtained using the methods described above, examples of the beryllium borate anionic group derived from borate anionic groups through $[BeO_4]$ substitution are scant. In our previous study, we reported the synthesis of the first alkaline beryllium borate $Na_2BeB_2O_5$[33] that contains $[BeB_2O_7]^{6-}$ groups derived from $[B_3O_7]^{5-}$ by $[BeO_4]$ substitution. While it crystallized in a centrosymmetric structure, this approach to beryllium borate anionic group construction was successful and will allow further advances in NLO materials development.

In this study, we carried out systematical synthesis based on the $A_2O-BeO-B_2O_3$ (A = Na, K, Rb) systems to obtain deep UV NLO crystals containing new beryllium borate anionic groups or frameworks. This has resulted in a series of new alkaline beryllium borates with the stoichiometry $NaBeB_3O_6$ and $ABe_2B_3O_7$ (A = K, Rb). For the first time, a new beryllium borate anionic group $[Be_2B_3O_{11}]^{9-}$ was found in the structure of $NaBeB_3O_6$ and α-$KBe_2B_3O_7$. *β*-$KBe_2B_3O_7$, *γ*-$KBe_2B_3O_7$, and $RbBe_2B_3O_7$ consist of 2D alveolate beryllium borate network $[Be_2BO_5]_\infty$ which were found in an anhydrous beryllium borate compound for the first time. Furthermore the adjacent $[Be_2BO_5]_\infty$ layers in these compounds were connected by covalent bonds. The synthesis, structures, thermal behaviors, spectra, and NLO properties of these borates were described in this paper.

2. Experimental Section

Reagents. Na_2CO_3 (99.8%), K_2CO_3 (99.0%), Rb_2CO_3 (99.5%), BeO (99.5%), and B_2O_3 (99.5%) were purchased from Sinopharm and used as received.

Syntheses of Alkaline Beryllium Borate Crystals. Due to the toxicity of BeO, all of the experiments were performed in a ventilated system. Single crystals of $NaBeB_3O_6$ were grown from a high temperature solution by using $Na_2O-3B_2O_3$ as a flux. This solution was prepared in a platinum crucible by melting a mixture of Na_2CO_3, BeO, and B_2O_3 at a molar ratio of $Na_2O/BeO/B_2O_3$ = 1:0.5:3. The mixture (10 g) was heated in a programmable temperature electric furnace at 1050 °C until the melt became transparent and clear. The homogenized melt solution was then cooled rapidly (50 °C/h) to the initial crystallization temperature (800 °C). It was further cooled slowly (3 °C/h) to the final crystallization temperature (650 °C) and then allowed to cool to room temperature by powering off the furnace. The flux attached to the crystal was readily dissolved in water.

Similarly, single crystals of $ABe_2B_3O_7$ (A = K, Rb) were grown by spontaneous crystallization with alkaline borates as the flux. Moreover, by varying the crystallization temperature, three phases of polymorphous $KBe_2B_3O_7$ crystals were obtained, which were not observed for the case of rubidium crystals. The three phases of polymorphous $KBe_2B_3O_7$ crystals were referred to as α-, *β*-, and *γ*-$KBe_2B_3O_7$. The molar ratios of the melt mixtures for growing α-, *β*-, and *γ*-$KBe_2B_3O_7$ were $K_2O/BeO/B_2O_3$ = 1:0.8:3, 1:0.7:3, and 1:0.6:3, respectively. The three phases were obtained by crystallizing the melts at 770, 750, and 730 °C, for α-, *β*-, and *γ*-$KBe_2B_3O_7$, respectively, for 24 h and then were quenched in the air by taking the crucibles out of the furnace. The flux attached to the crystal was readily dissolved and removed in water.

Single Crystal X-ray Diffraction. Single crystal X-ray diffraction data were collected at room temperature on a Rigaku Mercury CCD diffractometer with graphite-monochromatic Mo Kα radiation (λ = 0.71073 Å). A transparent block of crystal was mounted on a glass fiber with epoxy for structure determination. A hemisphere of data was collected using a narrow-frame method with the ω-scan mode. The data were integrated using the CrystalClear program, and the intensities were corrected for Lorentz polarization, air absorption, and absorption attributable to the variation in the path length through the detector faceplate. Absorption corrections based on the Multiscan technique were also applied. The structure was solved by direct methods using SHELXS-97 and then refined by full-matrix least-squares refinement on F^2 with SHELXL-97[34] found in the software suite WinGX[35] v1.80.05. All of the structures were verified using the ADDSYM algorithm from the program PLATON,[36] and no higher symmetries were found. Relevant crystallographic data and details of the experimental conditions for

(15) Schaffers, K. I.; Keszler, D. A. *J. Solid State Chem.* **1990**, *85*, 270.
(16) Schaffers, K. I.; Keszler, D. A. *Inorg. Chem.* **1994**, *33*, 1201.
(17) Schaffers, K. I.; Keszler, D. A. *Acta Crystallogr., Sect. C: Cryst. Struct. Commun.* **1993**, *49*, 647.
(18) Luce, J. L.; Schaffers, K. I.; Keszler, D. A. *Inorg. Chem.* **1994**, *33*, 2453.
(19) Wen, X. H.; Li, R. K.; Chen, C. T. *Acta Crystallogr., Sect. C: Cryst. Struct. Commun.* **2006**, *62*, I21.
(20) Zachariasen, W. H. *Z. Kristallogr.* **1931**, *76*, 289.
(21) Zachariasen, W. H.; Plettinger, H. A.; Marezio, M. *Acta Crystallogr.* **1963**, *16*, 1144.
(22) Baidina, I. A.; Bakakin, V. V.; Podberezskaya, N. V.; Alekseev, V. I.; Batsanova, L. R.; Pavlyuchenko, V. S. *J. Struct. Chem.* **1978**, *19*, 105.
(23) Mei, L. F.; Wang, Y. B.; Chen, C. T. *Mater. Res. Bull.* **1994**, *29*, 81.
(24) Mei, L.; Huang, X.; Wang, Y.; Wu, Q.; Wu, B.; Chen, C. *Z. Kristallogr.* **1995**, *210*, 93.
(25) McMillen, C. D.; Kolis, J. W. *J. Cryst. Growth* **2008**, *310*, 2033.
(26) Chen, C. T.; Luo, S. Y.; Wang, X. Y.; Wang, G. L.; Wen, X. H.; Wu, H. X.; Zhang, X.; Xu, Z. Y. *J. Opt. Soc. Am. B* **2009**, *26*, 1519.
(27) McMillen, C. D.; Hu, J.; VanDerveer, D.; Kolis, J. W. *Acta Crystallogr., Sect. B: Struct. Sci.* **2009**, *65*, 445.
(28) Chen, C. T.; Wang, G. L.; Wang, X. Y.; Xu, Z. Y. *Appl. Phys. B: Lasers Opt.* **2009**, *97*, 9.
(29) Chen, C. T.; Wang, Y. B.; Wu, B. C.; Wu, K. C.; Zeng, W. L.; Yu, L. H. *Nature* **1995**, *373*, 322.
(30) Qi, H.; Chen, C. T. *Inorg. Chem. Commun.* **2001**, *4*, 565.
(31) Qi, H.; Chen, C. T. *Chem. Lett.* **2001**, 352.
(32) Chen, C. T.; Bai, L.; Wang, Z. Z.; Li, R. K. *J. Cryst. Growth* **2006**, *292*, 169.
(33) Li, W.; Ye, N. *Acta Crystallogr., Sect. E.: Struct. Rep. Online* **2007**, *63*, I160.
(34) Sheldrick, G. M. *Acta Crystallogr., Sect. A: Found. Crystallogr.* **2008**, *64*, 112.
(35) Farrugia, L. J. *J. Appl. Crystallogr.* **1999**, *32*, 827.
(36) Spek, A. L. *J. Appl. Crystallogr.* **2003**, *36*, 7.

Table 1. Crystal Data and Structure Refinement for $NaBeB_3O_6$ and $ABe_2B_3O_7$ (A = K, Rb)[a]

formula	$NaBeB_3O_6$	α-$KBe_2B_3O_7$	β-$KBe_2B_3O_7$	γ-$KBe_2B_3O_7$	$RbBe_2B_3O_7$
formula mass (amu)	160.43	201.55	201.55	604.65	247.92
crystal system	orthorhombic	monoclinic	orthorhombic	monoclinic	orthorhombic
space group	$Pna2_1$	$C2/c$	$Pmn2_1$	$P2_1$	$Pmn2_1$
a (Å)	9.153(6)	10.405(10)	7.639(6)	7.4766(13)	7.687(4)
b (Å)	11.934(8)	9.001(7)	17.464(13)	13.2701(18)	17.724(9)
c (Å)	4.372(3)	6.559(14)	4.376(3)	9.3263(17)	4.393(2)
β (deg)		114.543(11)		111.272(10)	
V (Å^3)	477.6(5)	558.8(14)	583.8(7)	862.3(2)	598.5(5)
Z	4	4	4	2	4
crystal size (mm^3)	0.25 × 0.06 × 0.04	0.4 × 0.35 × 0.1	0.4 × 0.4 × 0.05	0.2 × 0.1 × 0.05	0.15 × 0.15 × 0.03
ρ(calcd) (g/cm^3)	2.231	2.396	2.293	2.329	2.751
temperature (K)	293(2)	293(2)	293(2)	293(2)	293(2)
λ (Å)	0.71073	0.71073	0.71073	0.71073	0.71073
F(000)	312	392	392	588	464
μ (mm^{-1})	0.28	0.934	0.894	0.908	8.257
θ (deg)	2.8−27.49	3.12−27.46	2.33−27.47	2.34−27.47	2.3−27.45
index range	$-11 \le h \le 11$ $-15 \le h \le 11$ $-5 \le h \le 5$	$-10 \le h \le 13$ $-11 \le h \le 11$ $-8 \le h \le 8$	$-9 \le h \le 9$ $-22 \le h \le 22$ $-5 \le h \le 5$	$-9 \le h \le 9$ $-17 \le h \le 17$ $-12 \le h \le 10$	$-9 \le h \le 9$ $-22 \le h \le 22$ $-5 \le h \le 5$
R_{int}	0.0422	0.0242	0.0284	0.023	0.0468
reflections collected	3530	2070	4249	6720	4448
reflections ($I > 2\sigma(I)$)/ independent reflections	999/1100	565/608	1361/1431	3031/3443	1227/1409
data/restraints/ parameters	1100/1/102	608/0/62	1431/1/130	3443/1/352	1409/1/131
R/wR ($I > 2\sigma(I)$)	0.0378/0.0741	0.0235/0.0612	0.0271/0.0675	0.0405/0.1141	0.0338/0.074
R/wR (all data)	0.0438/0.0763	0.0244/0.0619	0.029/0.069	0.0465/0.1195	0.04/0.0767
GOF on F^2	1.11	1.171	1.067	1.092	1.012
Flack parameter	0.4(6)	N/A	−0.03(5)	0.00(6)	0.004(15)
largest diff. peak and hole (e/Å^{-3})	0.215 and −0.226	0.259 and −0.36	0.269 and −0.425	0.853 and −0.88	0.895 and −1.062

[a] $R(F) = \sum||F_o| - |F_c||/\sum|F_o|$. $wR(F_o^2) = [\sum w(F_o^2 - F_c^2)^2/\sum w(F_o^2)^2]^{1/2}$.

$NaBeB_3O_6$, α-$KBe_2B_3O_7$, β-$KBe_2B_3O_7$, γ-$KBe_2B_3O_7$, and $RbBe_2B_3O_7$ are summarized in Table 1. Atomic coordinates and isotropic displacement coefficients are listed in Tables S1−S5 in the Supporting Information.

Powder X-ray Diffraction. X-ray diffraction patterns of polycrystalline materials were obtained on a Rigaku Dmax2500 powder X-ray diffractometer by using Cu Kα radiation ($\lambda = 1.540598$ Å) at room temperature in the angular range of $2\theta = 0°-60°$ with a scan step width of 0.05° and a fixed time of 0.2 s. The powder XRD patterns for $NaBeB_3O_6$, α-$KBe_2B_3O_7$, β-$KBe_2B_3O_7$, γ-$KBe_2B_3O_7$, and $RbBe_2B_3O_7$ showed good agreement with the calculated XRD patterns from the single-crystal models.

Element Analysis. Element analysis of the crystals was performed by using a Jobin Yvon Ultima2 inductively coupled plasma optical emission spectrometer (ICP-OES) with Sepex Certiprep standards. The crystal samples were dissolved in a mixture of nitric acid (3 mL) and hydrochloric acid (3 mL).

Differential Thermal Analysis. Differential thermal analysis (DTA) scans were measured on a NETZSCH STA 449C simultaneous analyzer. Reference (Al_2O_3) and crystal samples (5−15 mg) were enclosed in Al_2O_3 crucibles and heated from room temperature to 1100 °C at a rate of 15 °C/min under a constant flow of nitrogen gas. The DTA residues were visually inspected and then analyzed by X-ray powder diffraction after the experiments.

UV−vis Diffuse Reflectance Spectroscopy. The UV−vis diffuse reflection data were recorded at room temperature using a powder sample with $BaSO_4$ as a standard (100% reflectance) on a PerkinElmer Lamda-900 UV/vis/NIR spectrophotometer over the spectra range 200−800 nm. Reflectance spectra were converted to absorbance using the Kubelka−Munk function.[37,38]

Second-Harmonic Generation. Powder second-harmonic generation (SHG) signals were measured using the experimental method adapted from Kurtz and Perry.[39] Since SHG efficiencies are known to depend strongly on particle size, polycrystalline samples were ground and sieved into the following particle size ranges: 20−44, 44−74, 74−105, 105−149, and 149−210 μm. To make relevant comparisons with known SHG materials, crystalline LBO was also ground and sieved into the same particle size ranges. The samples were pressed between glass microscope cover slides and secured with tape in 1-mm thick aluminum holders containing an 8-mm diameter hole. They were then placed in a light-tight box and irradiated with a pulsed infrared beam (10 ns, 3 mJ, 10 Hz) from a Q-switched Nd:YAG laser of wavelength 1064 nm. A cutoff filter was used to limit background flash-lamp light on the sample, and an interference filter (530 ± 10 nm) was used to select the second harmonic for detection with a photomultiplier tube attached to a RIGOL DS1052E 50-MHz oscilloscope. This procedure was then repeated using the standard nonlinear optical material LBO, and the ratio of the second-harmonic intensity outputs was calculated. No index-matching fluid was used in any of the experiments.

3. Results and Discussion

3.1. Crystal Growth and Thermal Behavior. We have successfully synthesized a new series of alkaline beryllium borate

(37) Kubelka, P.; Munk, F. *Z. Tech. Phys* **1931**, *12*, 593.
(38) Tauc, J. *Mater. Res. Bull.* **1970**, *5*, 721.
(39) Kurtz, S. K.; Perry, T. T. *J. Appl. Phys.* **1968**, *39*, 3798.

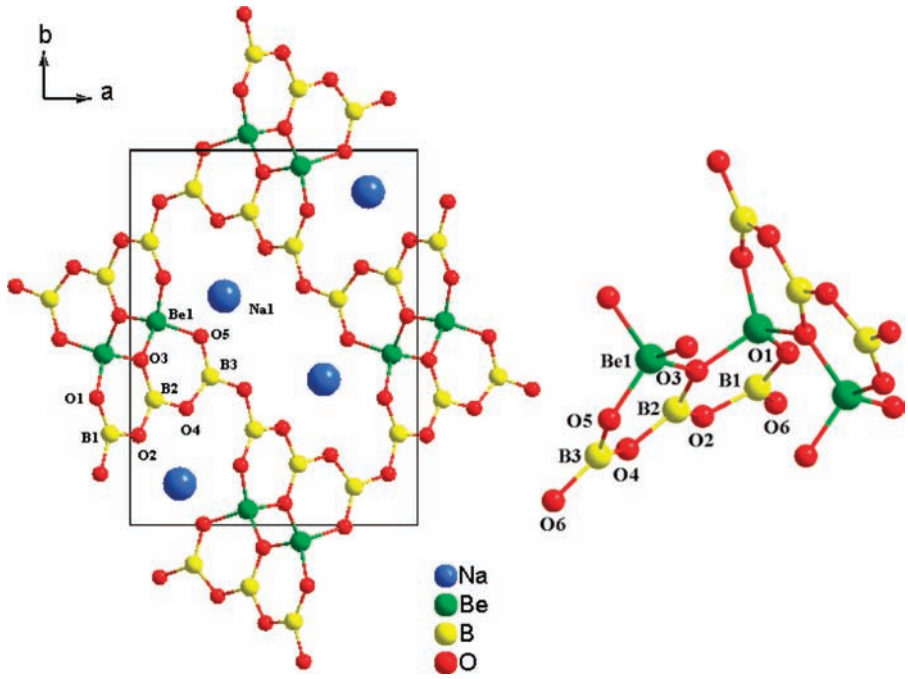

Figure 1. Crystal structure of $NaBeB_3O_6$ and the connections of the anionic group $[Be_2B_3O_{11}]^{9-}$ in the structure.

crystals of $NaBeB_3O_6$ and $ABe_2B_3O_7$ (A = K, Rb) based on the $A_2O-BeO-B_2O_3$ (A = Na, K, Rb) system. As shown in Figure S1, the DTA curves for $NaBeB_3O_6$ exhibit only one endothermic peak beginning at 866 °C upon heating to 1100 °C (see Supporting Information Figure S1). Analysis of the powder XRD pattern of the residues revealed that $NaBeB_3O_6$ was decomposed into $Be_3B_2O_6$,[40] demonstrating that $NaBeB_3O_6$ is an incongruently melting compound. Therefore, large crystals of $NaBeB_3O_6$ must be grown with flux and below the decomposition temperature.

As shown in Figure S1, the DTA results indicate that the thermal behaviors of $ABe_2B_3O_7$ (A = K, Rb) were different from that of $NaBeB_3O_6$. There were two endothermic peaks for each curve as the samples were being heated. The first endothermic peak beginning at 899 °C (α-$KBe_2B_3O_7$), 875 °C (β-$KBe_2B_3O_7$), 853 °C (γ-$KBe_2B_3O_7$), and 851 °C ($RbBe_2B_3O_7$) corresponded to the decomposition of $ABe_2B_3O_7$ into $ABe_4B_3O_9$ (A = K, Rb[19]). The second endothermic peak beginning at 970 °C (α-$KBe_2B_3O_7$), 970 °C (β-$KBe_2B_3O_7$), 977 °C (γ-$KBe_2B_3O_7$), and 990 °C ($RbBe_2B_3O_7$) corresponded to the decomposition of $ABe_4B_3O_9$ into $Be_3B_2O_6$ and BeO. These phase transition reactions were further confirmed by XRD analysis of sample residues that were heated at 900 °C (24 h) and then at 1000 °C (24 h) and then quenched quickly to room temperature. No obvious peaks were observed on the DTA curves that would correspond to the phase transitions between α-, β-, and γ-$KBe_2B_3O_7$, which were expected to occur between 700 and 800 °C as the crystallization temperatures used to generate these polymorphous $KBe_2B_3O_7$ crystals. This may be explained by the samples being over heated under the relatively high heating rate of the DTA equipment. In fact, the overheated metastable β- and γ-phases decomposed directly into $ABe_4B_3O_9$ at different temperatures, which did not allow us to observe directly the γ- to β-phase and β- to α-phase transitions. Long-term annealing experiments supported the relationships among these three phases. The XRD patterns indicated that the powder of β-$KBe_2B_3O_7$ changed to α-$KBe_2B_3O_7$ after annealing for 24 h at 770 °C.

Transparent and colorless $NaBeB_3O_6$ and $ABe_2B_3O_7$ crystals have been grown by spontaneous crystallization in a molten flux based on the self-fluxed system $A_2O-3B_2O_3$. They are all chemically stable with respect to water.

Since the polymorphous behaviors of $KBe_2B_3O_7$ are temperature dependent, each crystal phase was grown at a fix temperature followed by a rapid cooling process after precipitation of the desired crystallization phase instead of slow cooling to avoid phase transitions that can occur during a slow cooling process. However, because the optimal crystallization temperatures of the three phases are so close, the main product was obtained with a minor amount of other phases at each crystallization temperature. In fact, we obtained α-phase with 30% β-phase at 770 °C, β-phase with traces of α- and γ-phases at 750 °C, and γ-phase with a trace of β-phase at 730 °C, respectively. These crystals of different phases were sorted based on their different morphologies. Pictures of $NaBeB_3O_6$ and $ABe_2B_3O_7$ (A = K, Rb) crystals are shown in Figure S2 in the Supporting Information.

3.2. Crystal Structure. $NaBeB_3O_6$ crystallizes into an orthorhombic crystal system with an acentric space group of $Pna2_1$. The structure is illustrated along the *c*-axis in Figure 1. The B atoms are coordinated to three O atoms to form planar $[BO_3]$ triangles with B−O bond lengths ranging from 1.319(3) to 1.399(3) Å and O−B−O bond angles ranging from 110.9(2)° to 126.6(2)°. The Be atoms are bound to four O atoms to form distorted $[BeO_4]$ tetrahedra with Be−O bond lengths ranging from 1.597(4) to 1.669(3) Å and O−Be−O bond angles from 107.09(19)° to 113.1(2)°. All O atoms are 2-fold coordinated except O3, which is 3-fold coordinated. In the $NaBeB_3O_6$ structure, three $[BO_3]$ triangles and two $[BeO_4]$ tetrahedra share their vertexes to form a nearly coplanar double six-membered ring $[Be_2B_3O_{11}]^{9-}$, which is similar to a naphthalene molecule and not observed before from other borate compounds (Figure

(40) Blackburn, P. E.; Büchler, A. *J. Phys. Chem.* **1965**, *69*, 4250.

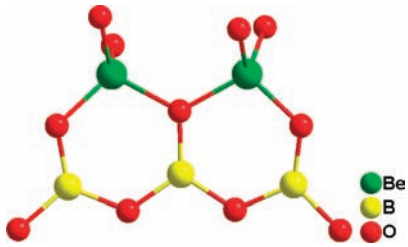

Figure 2. Anionic group $[Be_2B_3O_{11}]^{9-}$.

2). The adjacent $[Be_2B_3O_{11}]^{9-}$ building blocks are connected vertically by sharing their $[BeO_4]$ tetrahedra to form endless cruciate chains along the *c*-axis. The adjacent cruciate chains are connected to each other by sharing the O6 atoms from $[BO_3]$ triangles to build tunnels along the *c*-axis, resulting in the final three-dimensional (3D) open framework. Na^+ cations are located in the tunnels and a 5 + 1 coordination environment with one considerably longer Na−O bond of 2.980(3) Å. Being an NLO-active anionic group, the double six-member ring $[Be_2B_3O_{11}]^{9-}$ possesses a larger π-conjugated electron system than that of $[B_3O_7]^{5-}$ in LBO; consequently, it may have larger microscopy second-order susceptibility. Furthermore, the vertical alignment of $[Be_2B_3O_{11}]^{9-}$ groups to the *a*−*c* plane in the unit cell tends to have larger anisotropic linear polarization, i.e., larger birefringence. Therefore, $NaBeB_3O_6$ is a promising deep UV NLO crystal.

α-$KBe_2B_3O_7$ crystallizes in monoclinic crystal system with a centrosymmetric space group of *C*2/*c*. The structure is illustrated along the *c*-axis in Figure 3. In the structure, B atoms are coordinated to three O atoms to form planar $[BO_3]$ triangles with B−O bond lengths ranging from 1.331(2) to 1.410(2) Å and O−B−O bond angles ranging from 113.28(19)° to 123.36(10)°. The Be atoms are bound to four O atoms to form distorted $[BeO_4]$ tetrahedra with Be−O bond lengths ranging from 1.564(2) to 1.684(4) Å and O−Be−O angles from 92.45(10)° to 117.65(14)°. O1 and O2 atoms are 3-fold coordinated while O3 and O4 are 2-fold coordinated. The basic building block of α-$KBe_2B_3O_7$ is $[Be_2B_3O_{11}]^{9-}$, which was found in the structure of $NaBeB_3O_6$ as described above. The adjacent $[Be_2B_3O_{11}]^{9-}$ anionic groups are connected in a parallel formation from the opposite direction by sharing the edges of one of each $[BeO_4]$ tetrahedra to form a 3D open framework. K^+ cations reside in the cages of the framework and are located in an octa coordination environment with K−O bond lengths ranging from 2.781(3) to 2.858(5) Å. Although α-$KBe_2B_3O_7$ contains NLO-active $[Be_2B_3O_{11}]^{9-}$ groups, their centrosymmetric alignment results in the cancellation of NLO susceptibilities.

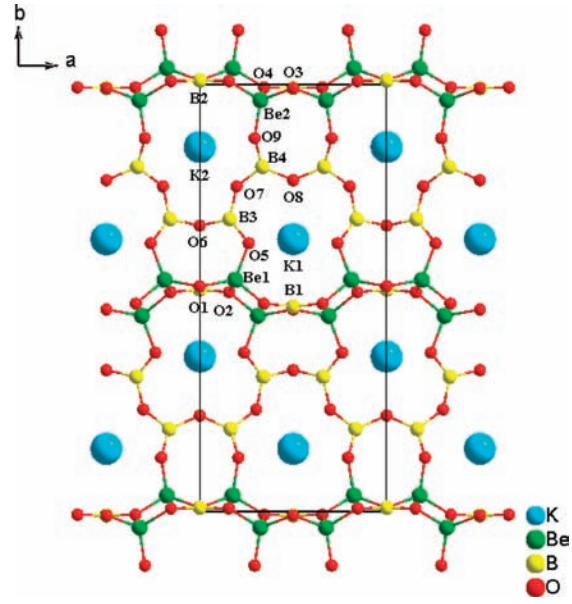

Figure 4. Crystal structure of β-$KBe_2B_3O_7$.

***β*-$KBe_2B_3O_7$** and **$RbBe_2B_3O_7$** are isostructural and crystallize into an orthorhombic crystal system with an acentric space group of $Pmn2_1$. Hence, only the structure of β-$KBe_2B_3O_7$ will be discussed in detail as a representation. The structure is illustrated along the *c*-axis in Figure 4. In the structure, both B atoms are coordinated to three O atoms to form planar $[BO_3]$ triangles with B−O bond lengths ranging from 1.307(3) to 1.394(3) Å and O−B−O bond angles ranging from 113.76(19)° to 128.3(2)°. The Be atoms are bound to four O atoms to form distorted $[BeO_4]$ tetrahedra with Be−O bond lengths ranging from 1.572(3) to 1.672(3) Å and O−Be−O angles from 106.11(15)° to 115.48(16)°. An extended 2D alveolate beryllium borate network $[Be_2BO_5]_\infty$ lying in the *a*−*c* plane was found in this

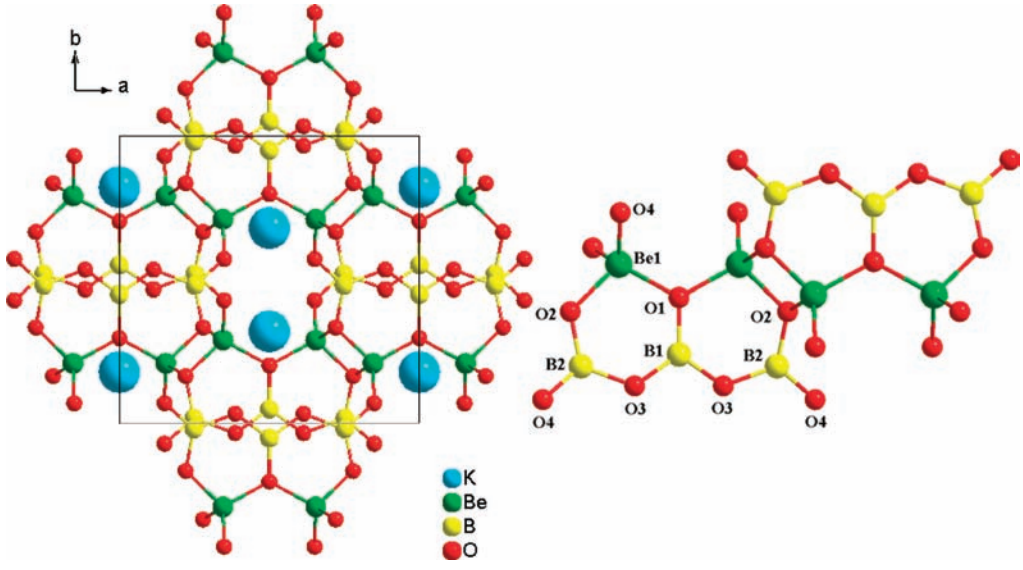

Figure 3. Crystal structure of α-$KBe_2B_3O_7$ and the connections of the anionic group $[Be_2B_3O_{11}]^{9-}$ in the structure.

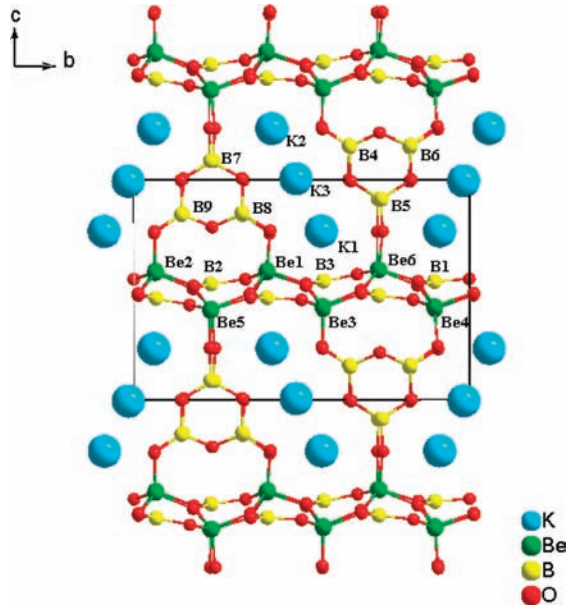

Figure 5. Crystal structure of γ-$KBe_2B_3O_7$.

structure, which was only found in a hydrated beryllium borate $Be_2BO_3OH \cdot H_2O$[20,21] previously. The adjacent $[Be_2BO_5]_\infty$ layers glide toward opposite directions along the *c*-axis. The layers are bridged by a parallel aligned one-dimensional (1D) metaborate chain $[BO_2]_\infty$ running along the *a*-axis that exists in lithium metaborate ($LiBO_2$),[41] by sharing O atoms (2-fold coordinated) to form a framework with two types of tunnels running through the *c*-axis. The K^+ cations reside in these tunnels, where $K1^+$ cations are located in a 9 coordination environment with K−O bond lengths ranging from 2.746(2) to 3.325(3) Å and $K2^+$ cations are located in a 7 + 1 coordination environment with one considerably longer K−O bond of 3.363(3) Å.

γ-$KBe_2B_3O_7$ crystallizes into a monoclinic crystal system with a chiral space group of $P2_1$. The structure along the *a*-axis is shown in Figure 5. In the structure, B atoms are coordinated to three O atoms to form planar $[BO_3]$ triangles with B−O bond lengths ranging from 1.293(4) to 1.421(6) Å and O−B−O bond angles ranging from 115.4(4)° to 123.7(4)°. The Be atoms are bound to four O atoms to form distorted $[BeO_4]$ tetrahedra with Be−O bond lengths ranging from 1.593(4) to 1.665(6) Å and O−Be−O angles from 104.5(3)° to 115.8(4)°. A similar 2D layer $[Be_2BO_5]_\infty$ to that of β-$KBe_2B_3O_7$ was found in γ-$KBe_2B_3O_7$, except the connection between the adjacent $[Be_2BO_5]_\infty$ layers are different. The adjacent layers lying in the *a*−*b* plane are bridged through $[B_3O_6]$ planar groups, which lay in the *b*−*c* plane and point in opposite directions from each other, by sharing O atoms (2-fold coordinated) to build a framework with three types of tunnels running through the *a*-axis. K^+ cations are found to reside in these tunnels, where $K1^+$ cations are located in a 9 coordination environment with K−O bond lengths ranging from 2.816(4) to 3.155(3) Å, $K2^+$ cations are located in a 9 + 1 coordination environment with one considerably longer K−O bond of 3.282(3) Å, and $K3^+$ cations are located in a 7 + 1 coordinated environment with one considerably longer K−O bond of 3.120(4) Å.

β- and γ-$KBe_2B_3O_7$ have similar structures; therefore, their nonlinearity originates from the same structure−property relationship. Although the network connectors, i.e., $[BO_2]_\infty$ chains and $[B_3O_6]$ groups in the β- and γ-phase, respectively, are NLO active building blocks, the sum of the their microscopic NLO susceptibilities are close to zero because they are related by an approximate center of symmetry in each structure. In contrast, as a common character of the coplanar beryllium borate network, $[BO_3]^{3-}$ groups in $[Be_2BO_5]_\infty$ layers of each phase have the same orientation (lower part of Figure 6), which is the optimal arrangement for producing large overall NLO properties. However, the distances between adjacent layers in the β-$KBe_2B_3O_7$ (8.73 Å) and γ-$KBe_2B_3O_7$ (8.70 Å) are longer than that in the KBBF[28] (6.25 Å), resulting in a lower $[BO_3]^{3-}$ density for the former. Therefore, the SHG coefficients of β-$KBe_2B_3O_7$ and γ-$KBe_2B_3O_7$ are predicted to be smaller than that of KBBF. Nevertheless, the strong connections provided by the covalent bonds between layers will eliminate drawbacks such as layer growth habit and cleavage that have limited the optical application for KBBF crystals.

The X-ray powder diffraction patterns of all of the compounds, grown crystals and the theoretical simulations from single crystal structures match each other very well. The differences in peak intensity for the same crystallographic index between the two patterns are believed to be caused by the preferred orientation of the powder samples (see Figure S3 Supporting Information).

The results of ICP elemental analysis of $NaBeB_3O_6$ and $ABe_2B_3O_7$ (A = K, Rb) (Table S6 Supporting Information) were consistent with the compositions determined from single crystal X-ray analysis.

3.3. Effect of Cation on Assembly of the Beryllium Borate Units. It is interesting that $NaBeB_3O_6$ adopts an acentric structure while α-$KBe_2B_3O_7$ adopts a centric structure, although they all have the common $[Be_2B_3O_{11}]^{9-}$ anionic group. The different connection modes of building blocks should originate from the difference in size of countering cations. Compared with larger K^+, Na^+ takes a lower coordination number. The requirement of Na^+ for a 6-fold coordination environment leads to the relatively compact connection of $[Be_2B_3O_{11}]^{9-}$ groups in $NaBeB_3O_6$ by sharing their $[BeO_4]$ tetrahedra. Owing to this acentric connection between $[Be_2B_3O_{11}]^{9-}$ groups (right part of Figure 1), the local acentric feature is constructively added to create an overall acentric extended structure.[6] In contrast, the 8-fold coordination environment of K^+ results in the loose connection of $[Be_2B_3O_{11}]^{9-}$ groups in α-$KBe_2B_3O_7$ by sharing the edges of their $[BeO_4]$ tetrahedra. In α-$KBe_2B_3O_7$, such a connection (right part of Figure 3) leads to a centric relation between adjacent $[Be_2B_3O_{11}]^{9-}$ groups, resulting in the cancellation of local NLO susceptibilities. Thus, it is interactions between the alkali metal and anionic group associated with the cation size that determine the macroscopic nonlinearity of materials.

The effect of cation size on the overall structure has also been observed in $KBe_2B_3O_7$ and $RbBe_2B_3O_7$. The former has two structural isomers, that is, β- and γ- phases, while for the latter only a single phase exists, which is isostructural to β-$KBe_2B_3O_7$. As mentioned above, in β-$KBe_2B_3O_7$ and $RbBe_2B_3O_7$, the $[Be_2BO_5]_\infty$ layers are bridged by flexible metaborate chains $[BO_2]_\infty$. Although the coordination sphere surrounding Rb^+ is different in size from that of K^+, this different requirement can be met through increasing or decreasing the bond angles of B−O−B and Be−O−B in the flexible $[BO_2]_\infty$ chains (Figure 4). One can find the angles of Be2−O9−B4 (146.33(19)°), B4−O7−B3 (137.93(19)°), and B3−O5−Be1 (118.78(15)°) in β-$KBe_2B_3O_7$ are smaller than those of $RbBe_2B_3O_7$ (152.0(4)°, 141.5(4)°, 121.2(4)°), respectively, leading to the changes of

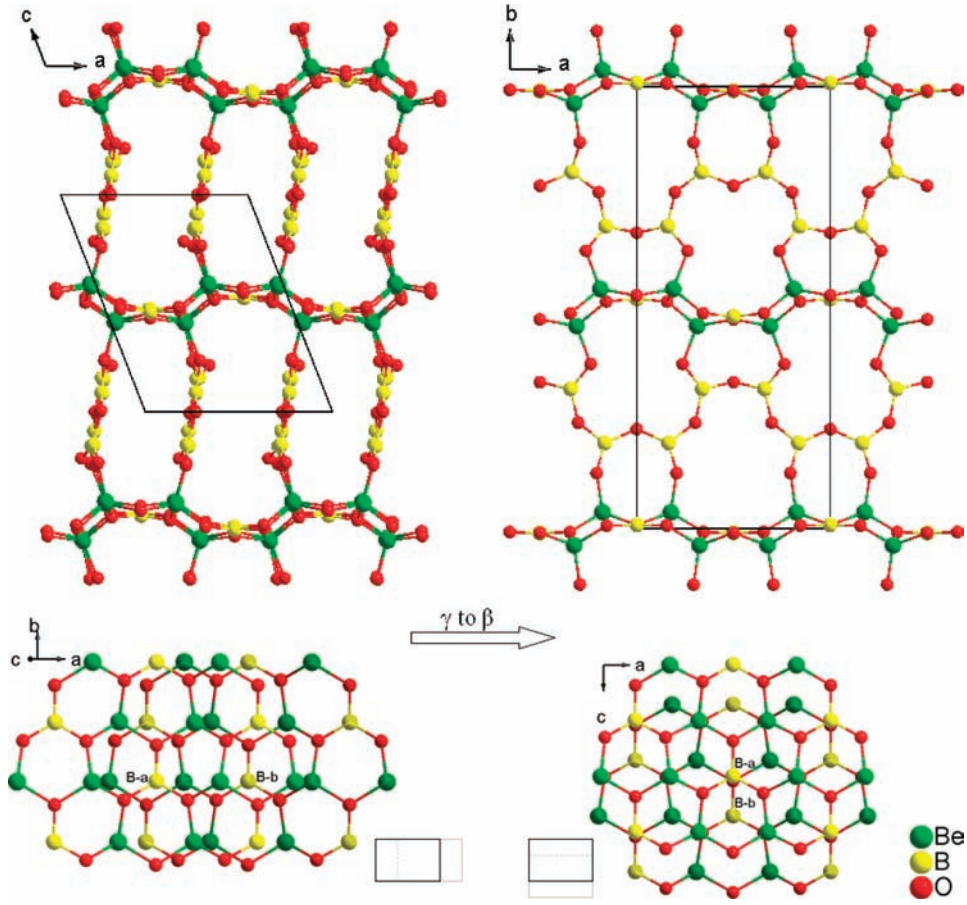

Figure 6. Structural evolution from γ-$KBe_2B_3O_7$ to β-$KBe_2B_3O_7$.

the distances between layers (β-$KBe_2B_3O_7$ (8.73 Å) and $RbBe_2B_3O_7$ (8.86 Å)). In γ-$KBe_2B_3O_7$, the adjacent layers (8.70 Å) are bridged by rigid $[B_3O_6]$ planar groups (Figure 5). However, the phase $RbBe_2B_3O_7$ that is isostructural to γ-$KBe_2B_3O_7$ does not exist because the rigid framework consisting of $[B_3O_6]$ is not able to be adjusted to accommodate a larger Rb^+ ion.

It is worth noting the transformation from a monoclinic β-phase to an orthorhombic γ-phase occurs as follows. Because there is only one unique orientation of $[BO_3]^{3-}$ groups in the $[Be_2BO_5]_\infty$ layers of the β- and γ- phase, the evolution of structure between them can be clearly explained by showing the structures with $[BO_3]^{3-}$ groups oriented in the same direction (Figure 6). When the γ-phase transforms into the β-phase, old B−O bonds of the $[B_3O_6]$ groups break and new B−O bonds form between the adjacent parallel $[Be_2BO_5]_\infty$ layers to build new $[BO_2]_\infty$ chains that extend vertically to the former $[B_3O_6]$ plane. Meanwhile, the adjacent $[Be_2BO_5]_\infty$ layers glide from each other along the $a-b$ plane. The driving force for the phase transformation may be attributed to the release of strain in the γ-phase. Compared with the β-phase in which layers are connected by flexible metaborate chains $[BO_2]_\infty$, the γ-phase in which layers are bridged by rigid $[B_3O_6]$ groups has higher strain and therefore is less stable. As a result, increasing temperature causes phase transformation of the γ-phase into the more stable β-phase.

3.4. Optical Properties. UV−vis diffuse reflectance spectra were collected for all of the reported compounds, except for α-$KBe_2B_3O_7$ (see Figure S4 in the Supporting Information). Absorption (K/S) data were calculated from the following Kubelka−Munk function:[37,38] $F(R) = (1 - R)^2/2R = K/S$, where R is the reflectance, K is the absorption, and S is the scattering. In the (K/S) versus E plots, extrapolating the linear part of the rising curve to zero provided the onset of absorption. No obvious absorption peak in the range of 6.22−1.55 eV (corresponding to 200−800 nm) was observed for $NaBeB_3O_6$, β-$KBe_2B_3O_7$, γ-$KBe_2B_3O_7$, and $RbBe_2B_3O_7$, indicating that these crystals may have potential use in deep UV NLO applications.

The curves of SHG signal as a function of particle size from the measurements made on ground crystals for $NaBeB_3O_6$, β-$KBe_2B_3O_7$, γ-$KBe_2B_3O_7$, and $RbBe_2B_3O_7$ are shown in Figure 7. The results are consistent with phase-matching behavior according to the rule proposed by Kurtz and Perry.[39] An LBO sample was selected as a reference to ensure the accuracy of measurements because it is an optical biaxial crystal, the same as the crystals to be measured. The second-harmonic signal was found to be 0.75, 0.35, 0.32, and 0.37 × LBO for $NaBeB_3O_6$, β-$KBe_2B_3O_7$, γ-$KBe_2B_3O_7$, and $RbBe_2B_3O_7$, respectively. These values are proportional to the squares of the nonlinear d_{eff} coefficients. Since the reported d_{eff} coefficient for LBO is 0.832 pm/V (2.133 × d_{36} (KDP)),[42] the derived d_{eff} coefficients for $NaBeB_3O_6$, β-$KBe_2B_3O_7$, γ-$KBe_2B_3O_7$, and $RbBe_2B_3O_7$ are 0.62, 0.29, 0.27, and 0.31 pm/V, which corresponded to approximately 1.60, 0.75, 0.68, and 0.79 times as large as that of d_{36} (KDP), respectively.

(41) Kirfel, A.; Will, G.; Stewart, R. F. *Acta Crystallogr., Sect. B: Struct. Sci.* **1983**, *39*, 175.
(42) Roberts, D. A. *IEEE J. Quantum Electron.* **1992**, *28*, 2057.

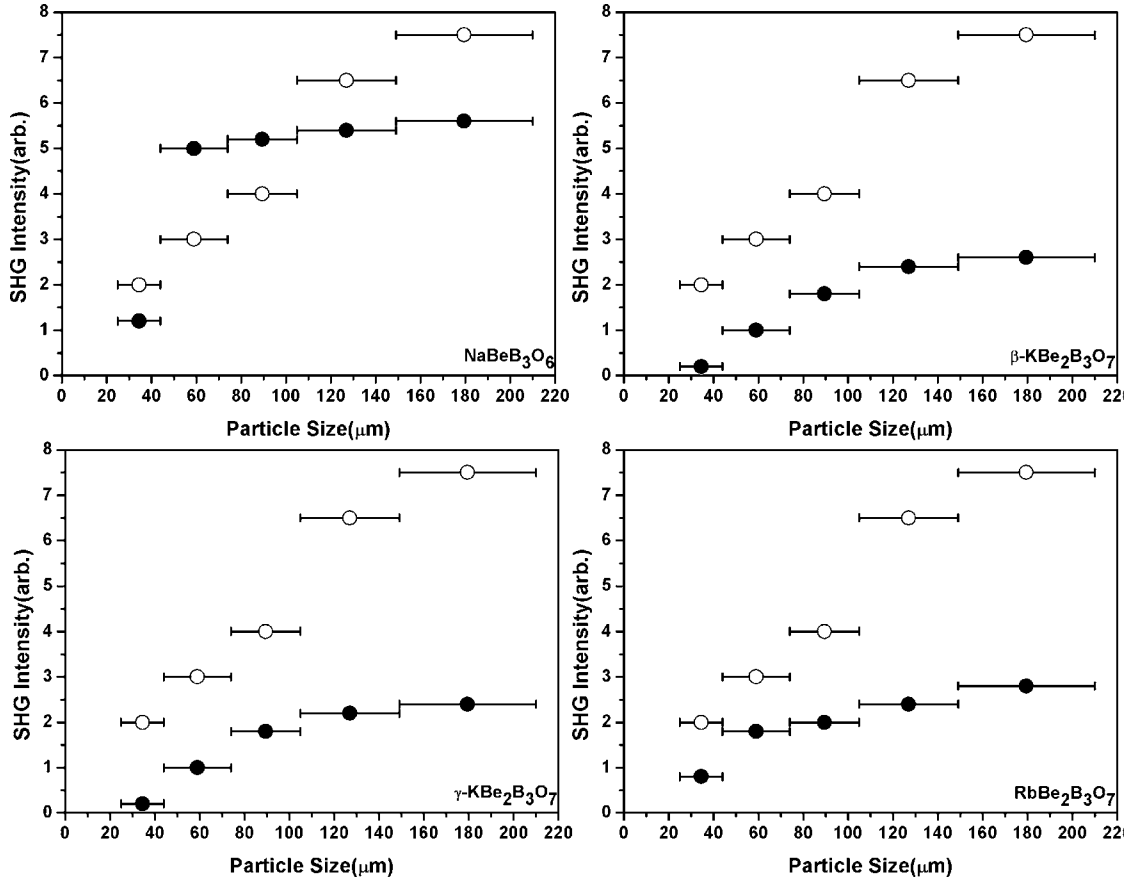

Figure 7. SHG measurements of $NaBeB_3O_6$, β-$KBe_2B_3O_7$, γ-$KBe_2B_3O_7$, and $RbBe_2B_3O_7$ ground crystals (●) with LBO (○) as a reference.

According to anionic group theory, the nonlinearity of β-$KBe_2B_3O_7$ and γ-$KBe_2B_3O_7$ relative to that of KBBF (1.115 $\times$ d_{36} (KDP))[28] should be determined by the number densities of $[BO_3]^{3-}$ groups in a unit cell, based on the same arrangement of the NLO-active $[BO_3]^{3-}$ groups and the same cations. The densities of $[BO_3]^{3-}$ groups were 0.00685 and 0.00696 per unit volume in β-$KBe_2B_3O_7$ and γ-$KBe_2B_3O_7$ respectively, which are less than that of KBBF (0.00946). Therefore, the nonlinearity values of β-$KBe_2B_3O_7$ and γ-$KBe_2B_3O_7$ were calculated to be 72.4% and 73.6% relative to KBBF, respectively. These results are approximately in accordance with the experimental values, which were 66.9% and 61.2% relative to KBBF for β-$KBe_2B_3O_7$ and γ-$KBe_2B_3O_7$, respectively. For the same reason, the density of $[BO_3]^{3-}$ groups in $RbBe_2B_3O_7$ (0.00668 per unit volume) is less than that of RBBF (0.00887). Furthermore, the nonlinearity of $RbBe_2B_3O_7$ was calculated to be 75.3% of RBBF (1.056 $\times$ d_{36} (KDP)),[26] while the experimental value was 74.7%.

4. Conclusions

A new series of alkaline beryllium borates $NaBeB_3O_6$, α-$KBe_2B_3O_7$, β-$KBe_2B_3O_7$, γ-$KBe_2B_3O_7$, and $RbBe_2B_3O_7$ have been synthesized using beryllium borate building block construction via substitution of a $[BeO_4]$ tetrahedron for $[BO_4]$. These novel borate crystals were obtained by spontaneous crystallization with molten flux based on $A_2O-B_2O_3$ (A = Na, K, Rb) solvent. The crystals were all noncentrosymmetric except α-$KBe_2B_3O_7$. $NaBeB_3O_6$ and α-$KBe_2B_3O_7$ consist of a new anionic group $[Be_2B_3O_{11}]^{9-}$, which is similar to naphthalene and is rarely found in inorganic matter. β-$KBe_2B_3O_7$ and $RbBe_2B_3O_7$ are isostructural. β-$KBe_2B_3O_7$, γ-$KBe_2B_3O_7$, and $RbBe_2B_3O_7$ consist of 2D alveolate beryllium borate layers $[Be_2BO_5]_\infty$ that are connected by strong covalent bonds. The characteristics of the three polymorphous phases of $KBe_2B_3O_7$ were determined by crystallization temperature, thermal behavior, and annealing experiment. The UV−vis diffuse reflectance spectroscopy on powder samples indicated that the short-wavelength absorption edges of these noncentrosymmetric materials are all below 200 nm. SHG on powder samples indicated that $NaBeB_3O_6$, β-$KBe_2B_3O_7$, γ-$KBe_2B_3O_7$, and $RbBe_2B_3O_7$ are all phase matchable materials, with measured SHG coefficients of approximately 1.60, 0.75, 0.68, and 0.79 times as large as that of d_{36} (KDP), respectively. These features make the alkaline beryllium borates very promising as deep UV NLO materials for practical applications.

Acknowledgment. This work was supported by the National Science Foundation of China (Nos. 50872132 and 90922035).

Supporting Information Available: DTA traces, crystal pictures, X-ray powder diffraction patterns, diffuse reflectance absorption curves, and crystal data (CIF). This material is available free of charge via the Internet at http://pubs.acs.org.

JA102737T